Supporting Information

Cobalt sulfides constructed heterogeneous interfaces decorated in N, S-codoped carbon nanosheets as highly efficient bifunctional oxygen electrocatalyst

Changbin Sun,[a] Jia Ding,[a] Haozhi Wang,[a] Jie Liu,[a] Xiaopeng Han,[a,b] Yida Deng,[a,b] Cheng Zhong[a,b,c*] and Wenbin Hu[a,b,c]

a Key Laboratory of Advanced Ceramics and Machining Technology (Ministry of Education), School of Materials Science and Engineering, Tianjin University, Tianjin 300072, China. Email: cheng.zhong@tju.edu.cn

b Tianjin Key Laboratory of Composite and Functional Materials, School of Materials Science and Engineering, Tianjin University, Tianjin 300072, China

c Joint School of National University of Singapore and Tianjin University, International Campus of Tianjin University, Binhai New City, Fuzhou 350207, China

Experimental Section

Structural Characterization: The morphologies of samples were observed by field-emission scanning electron microscopy (FESEM; S-4800, Hitachi), and high-resolution transmission electron microscopy (HRTEM; JEM-2100F, JEOL). The elemental compositions of the samples were analyzed by EDS mapping, which was attached to the TEM facility. The crystal structures of the samples were characterized by X-ray diffraction with Cu Kα radiation, λ = 0.1541 nm (XRD; D8 Advanced, Bruker Crop.). The specific surface area and pore structures were studied via an autosorb iQ instrument (Autosorb-iQ, Quantachrome) using Brumauer–Emmett–Teller (BET) and Barrett–Joyner–Halenda (BJH) method, respectively. The valence states of the samples were detected by X-ray photoelectron spectroscopy (XPS; Axis Supra, Kratos) with Al Kα radiation of 1486.6 eV.

Electrochemical Measurements: The oxygen reduction reaction (ORR) and oxygen evolution reaction (OER) electrochemical experiments were carried out on IviumStat and CHI660D electrochemical workstations at 25 °C, respectively. The standard three-electrode electrochemical cell consisted of a graphite rod counter electrode, a saturated calomel reference electrode (SCE) and a working electrode. For ORR test, the rotating ring-disk (RRDE) modified with catalyst ink was used as the working electrode (disk diameter is 5 mm, 0.196 cm^2). To prepare the catalyst ink, 7 mg prepared sample powders mixed with 3 mg carbon black was dispersed in a composite solution including 0.965 mL ethanol and 0.035 mL 5 wt% Nafion. Then the mixture was ultrasonically dispersed for 60 min to form a homogeneous catalyst ink. Subsequently, 15 μL as-

prepared ink was dropped on the electrode and dried at room temperature to obtain a mass loading of ~0.5 mg cm^{-2}. The ORR performance of catalysts was measured in O_2-saturated 0.1 M KOH solution. To fabricate the OER working electrodes, the slurry was deposited onto 1 × 1 cm^2 hydrophobic carbon cloth (mass loading of ~0.5 mg cm^{-2}) and dried at 60 °C for 4 h. The OER performance of catalysts was measured in O_2-saturated 1 M KOH solution. As comparison, the Pt/C (20 wt%) and IrO_2 electrodes were also fabricated with the same method. The linear sweep voltammetry (LSV) of ORR and OER was conducted at a scanning rate of 5 mV s^{-1} after scanning several cyclic voltammetry (CV) curves until the signals stabilized and the ring potential was constant at 1.5 V (vs. RHE) for ORR. Electrochemical impedance spectra were obtained under a frequency range of from 100 kHz to 10 mHz at 0.8 V for ORR or 1.5 V for OER (vs. RHE) with 10 mV amplitude of sinusoidal potential perturbation. The CV method was then adopted to evaluate the double layer capacitance.

To analyze the experimental data, all the potential was regularized with respect to the reversible hydrogen electrode (RHE) according to following equation: E (vs. RHE) = E (vs. SCE) + 0.059 ×pH + 0.241 V. The ORR and OER polarization measurements were iR-corrected through ohmic resistance of the solution determined by electrochemical impedance spectroscopy. The electron transfer number (n) and kinetic current density (J_K) were calculated via Koutecky–Levich (K–L) equation:[1]

$$\frac{1}{J} = \frac{1}{J_L} + \frac{1}{J_K} = \frac{1}{B\omega^{1/2}} + \frac{1}{J_K} \quad (1)$$

where J is the measured current density, J_L and J_K represent the diffusion-limiting and

kinetic-limiting current densities, respectively and ω is the rotation rate of electrode.

$$B = 0.62nFC_0D_0^{2/3}v^{-1/6} \quad (2)$$

Here, B can could be determined by the slope of the K–L curve, n represents the electron transfer number during the ORR process, F is the Faraday constant (96485 C mol^{-1}), C_0 is the O_2 concentration in the bulk solution (1.2×10^{-6} mol cm^{-3}), D_0 represents the diffusion coefficient of O_2 (1.9×10^{-5} cm^2 s^{-1}), in 0.1 M KOH, v is the kinematic viscosity of the electrolyte (0.01 cm^{-2} s^{-1}).[2]

For RRDEs, the percentage of peroxide species (y) and the electron transfer number (n) at 1600 rpm can be calculated by the following formulae:

$$y(\%) = 200 \times \frac{I_R/N}{I_D + I_R/N} \quad (3)$$

$$n = 4 \times \frac{I_D}{I_R/N + I_D} \quad (4)$$

where I_D and I_R are the disk and ring current, respectively, and N is the ring collection efficiency of RRDE (0.37).[3]

Assembly of aqueous zinc–air batteries: The zinc–air battery was constructed into a two-electrode configuration depending on the following procedure. The air-cathode electrode was prepared by loading the catalyst onto a hydrophobic carbon cloth (area: 1×1 cm^2, 1.05 mg cm^{-2}). A polished zinc plate was used as the anode (thickness: 0.5 mm) and 6 M KOH solution containing 0.2 M $Zn(Ac)_2$ (to ensure the reversible Zn anode reaction) was used as the electrolyte. Pt/C+IrO_2 mixed electrode was prepared by controlling the mass ratio of 1:1. The battery test was conducted by LAND-CT2001A testing devices.

Assembly of flexible solid zinc–air batteries: The structure of the flexible solid zinc–air battery contains polished zinc plate anode, solid electrolyte and $Co_9S_8/Co_{1-x}S$@NSC coated on hydrophobic carbon cloth cathode. The solid electrolyte was prepared by the following procedure. 3 g polyvinyl alcohol (PVA) was dissolved into 25 mL distilled water under stirring at 90 °C for 1.5 h followed by adding 6 ml 9 M KOH into above solution with continuous stirring for 20 min. Then the mixture was transferred into surroundings of −10 °C for 4 h to form PVA KOH gel. The air–cathode electrode was prepared by dropping the catalyst onto a hydrophobic carbon cloth (area: 1 × 2 cm^2, 1.05 mg cm^{-2}), which allowed O_2 to reach the catalyst sites from ambient air. The corresponding specific capacity (mAh g_{Zn}^{-1}) and energy density (Wh kg_{Zn}^{-1}) could be calculated by the following equations:

$$\text{Specific capacity} = \frac{\text{current} \times \text{service hours}}{\text{weight of consumed Zn}} \quad (5)$$

$$\text{Energy density} = \frac{\text{current} \times \text{service hours} \times \text{average discharge voltage}}{\text{weight of consumed Zn}} \quad (6)$$

Theoretical calculation: All the calculations were carried out within the framework of the density functional theory (DFT) via the Vienna Ab initio Simulation Package (VASP) code within the Perdew–Burke–Ernzerhof (PBE) generalized gradient approximation (GGA) and the projected augmented wave (PAW) method.[4-7] The cutoff energy for the plane-wave basis-set was set to 400 eV. The Brillouin zone of the surface unit cell was sampled by Monkhorst–Pack (MP) grids for $Co_{1-x}S$ and Co_9S_8 structure

optimizations.[8] A 2 × 1 supercell of the $Co_{1-x}S$(**Error!**10) surface and 2 × 2 supercell of the Co_9S_8(110) surface were constructed to model the catalyst in this work. The $Co_{1-x}S$(**Error!**10) and Co_9S_8(110) surfaces were determined by 3 × 2 × 1 and 2 × 2 × 1 Monkhorst−Pack grid. The convergence criterion for the electronic self-consistent iteration and force was set to 10^{-5} eV and 0.01 eV $Å^{-1}$, respectively. A vacuum layer of 12 Å was introduced to avoid interactions between periodic images.

The free energies of adsorbates at temperature T were evaluated based on the harmonic approximation, and the entropy is estimated by the following equation:[9, 10]

$$S(T) = k_B \sum_{i}^{\text{harm DOF}} \left[\frac{\varepsilon_i}{k_B T\left(e^{\varepsilon_i/k_B T} - 1\right)} - \ln\left(1 - e^{-\varepsilon_i/k_B T}\right) \right] \tag{7}$$

where k_B represents Boltzmann's constant and DOF is denoted as the degree of freedom. Meanwhile, the free energies of gas phase species are corrected as:

$$G_g(T) = E_{elec} + E_{ZPE} + \int C_p dT - TS(T) \tag{8}$$

where C_p represents the gas phase heat capacity as a function of temperature originated from Shomate equations and the corresponding parameters in the equations were obtained from National Institute of Standards and Technology (NIST).

The ORR reaction mechanism under alkaline conditions is generally accepted by following process:[11]

$$O_2(g) + * + e^- + H_2O(l) \rightarrow OOH^* + OH^- \tag{9}$$

$$OOH^* + e^- \rightarrow O^* + OH^- \tag{10}$$

$$O^* + H_2O(l) + e^- \rightarrow OH^* + OH^- \tag{11}$$

$$OH^* + e^- \rightarrow OH^- + * \tag{12}$$

The OER reaction mechanism follows the opposite process.

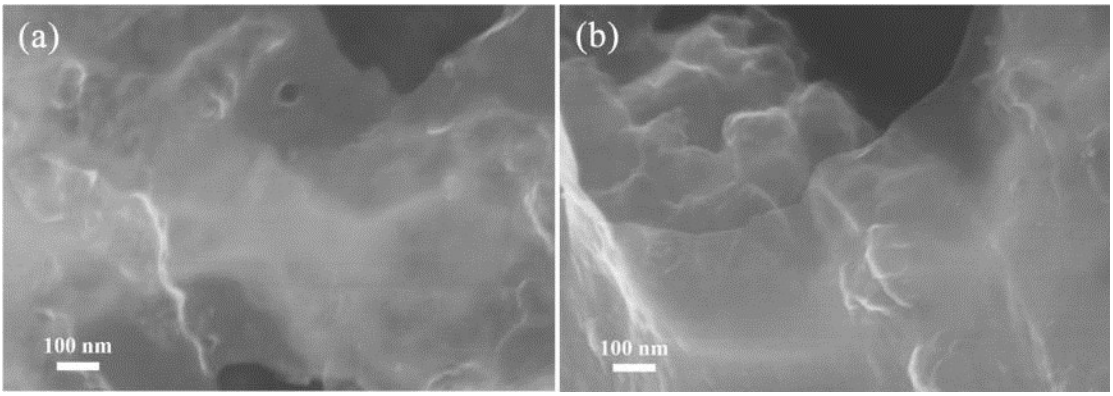

Fig. S1. SEM images of a) Co_9S_8@NSC and b) NSC samples.

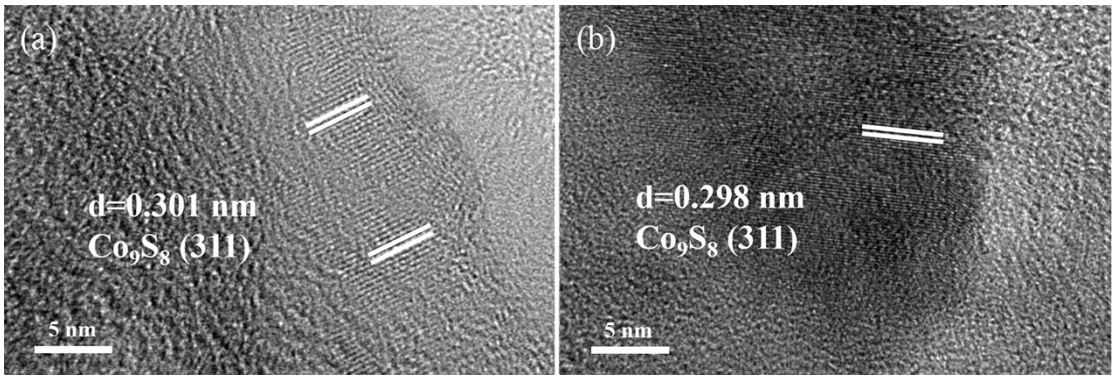

Fig. S2. HRTEM images of Co_9S_8@NSC nanosheets.

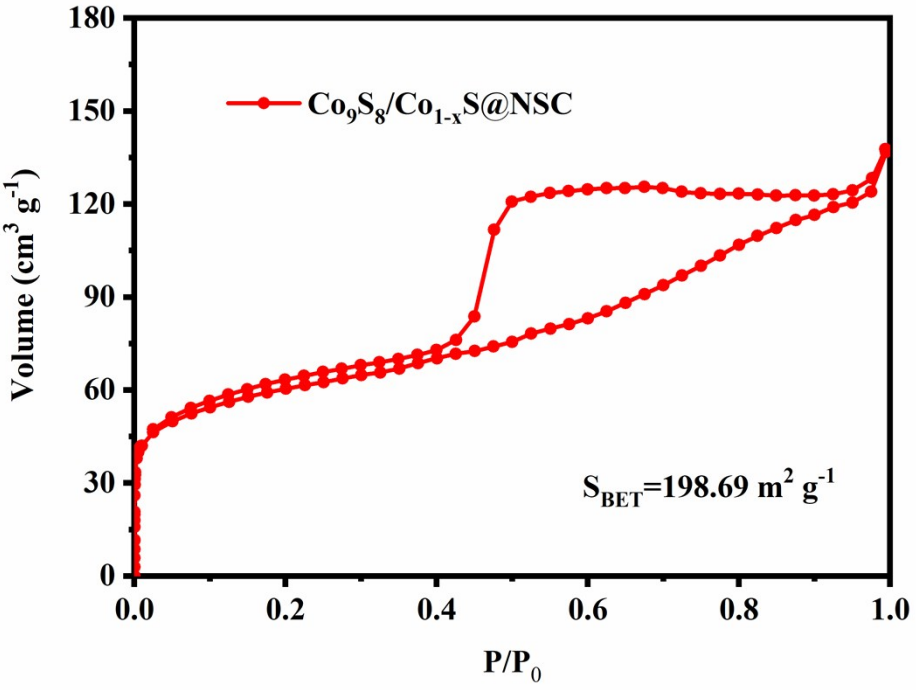

Fig. S3 N_2 adsorption-desorption isotherm curves of $Co_9S_8/Co_{1-x}S$@NSC sample.

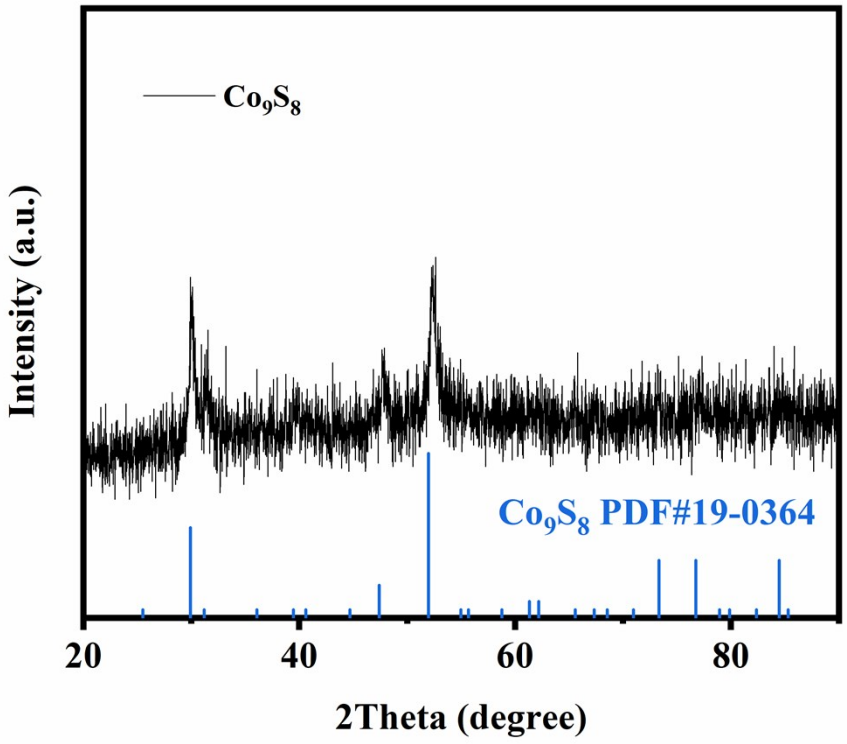

Fig. S4. XRD pattern of Co_9S_8 sample.

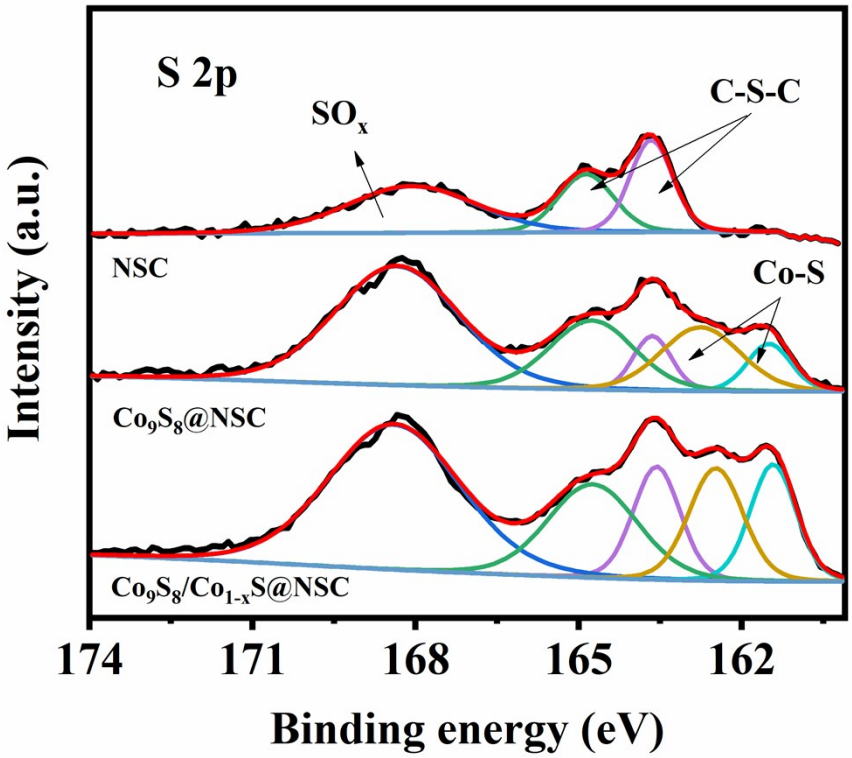

Fig. S5. The S 2p high-resolution XPS spectra of NSC, Co_9S_8@NSC and $Co_9S_8/Co_{1-x}S$@NSC samples.

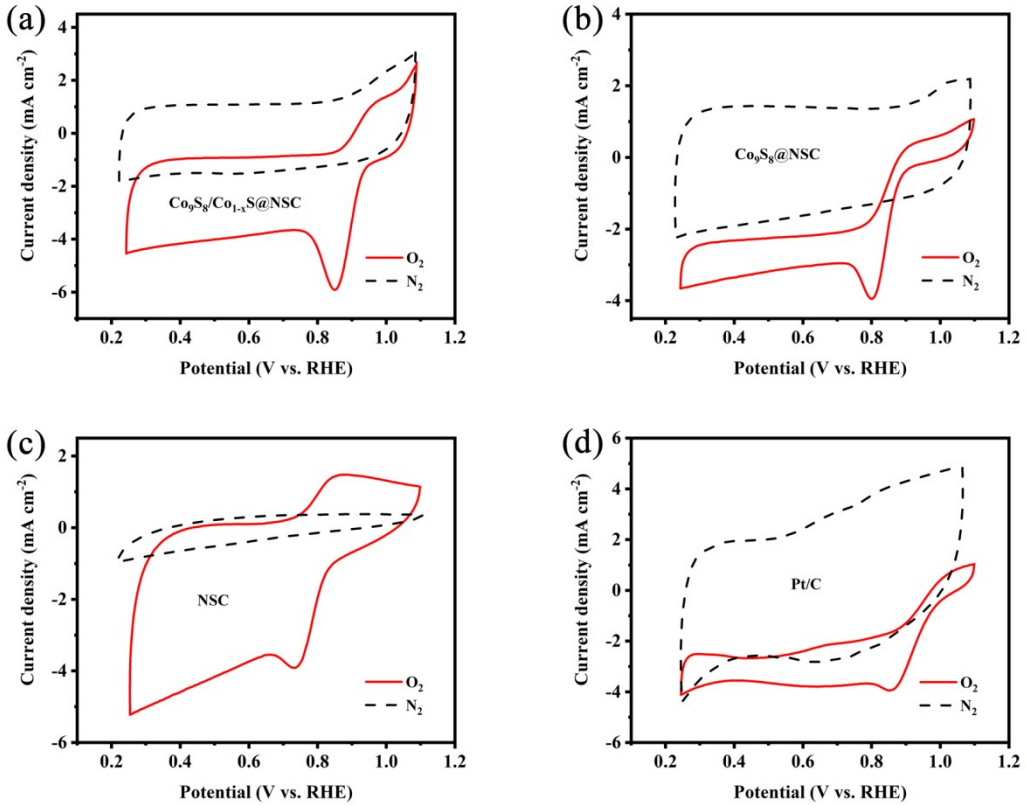

Fig. S6. Cycle voltammograms of a) $Co_9S_8/Co_{1-x}S$@NSC, b) Co_9S_8@NSC, c) NSC and (d) Pt/C samples in O_2-and N_2-saturated 0.1 M KOH at 50 mV s^{-1}.

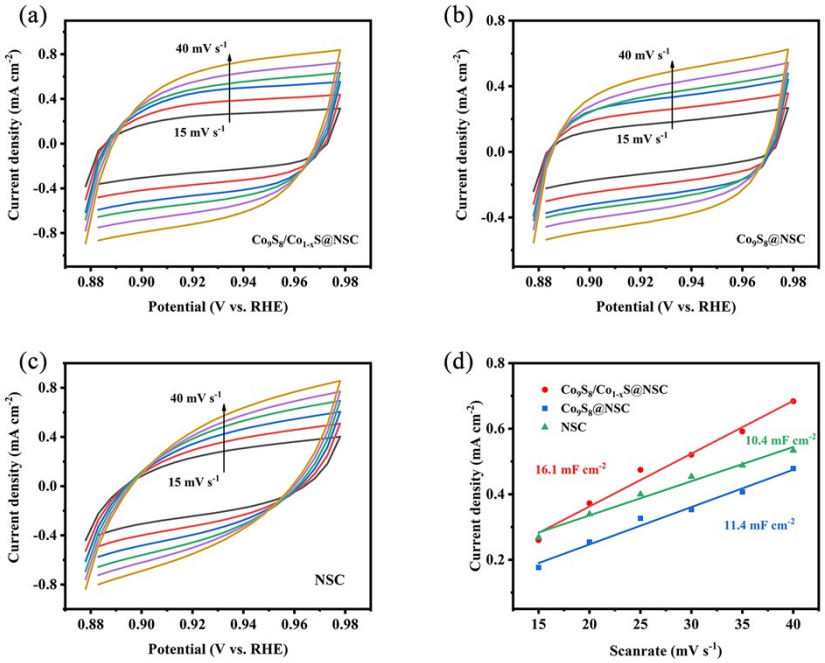

Fig. S7. Cycle voltammograms from 0.88 to 0.98 V vs. RHE for a) $Co_9S_8/Co_{1-x}S$@NSC, b) Co_9S_8@NSC and c) NSC samples in 0.1 M KOH at scan rates of 15, 20, 25, 30, 35 and 40 mV s^{-1}, respectively. d) Dependence of current densities as a function of scan rates for three samples.

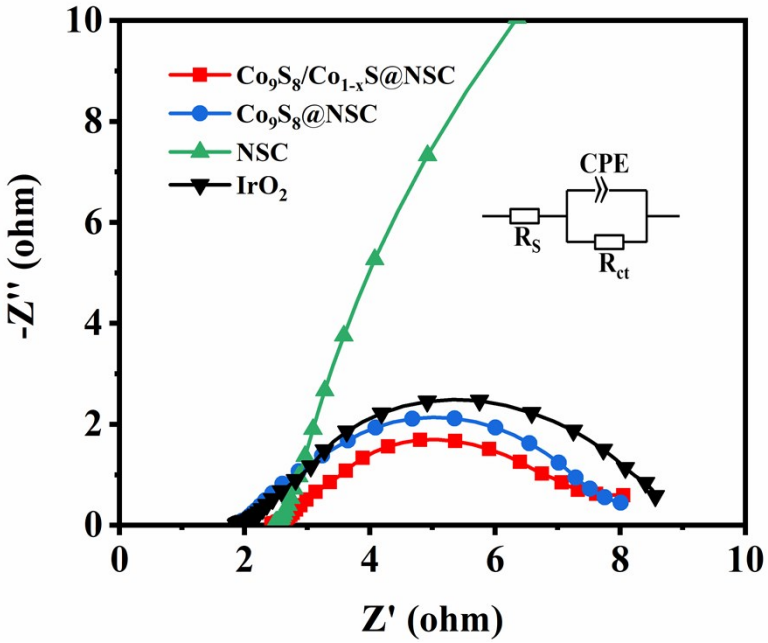

Fig. S8. Electrochemical impedance spectroscopy plots at 1.5 V (vs. RHE) of $Co_9S_8/Co_{1-x}S$@NSC, Co_9S_8@NSC, NSC, and IrO_2 samples for OER.

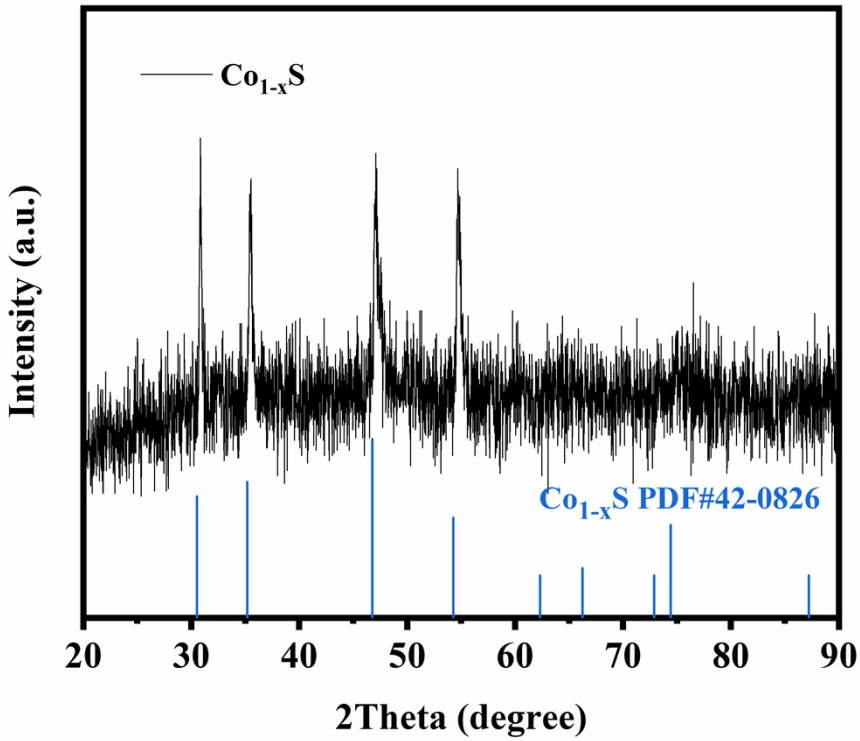

Fig. S9. XRD pattern of $Co_{1-x}S$ sample.

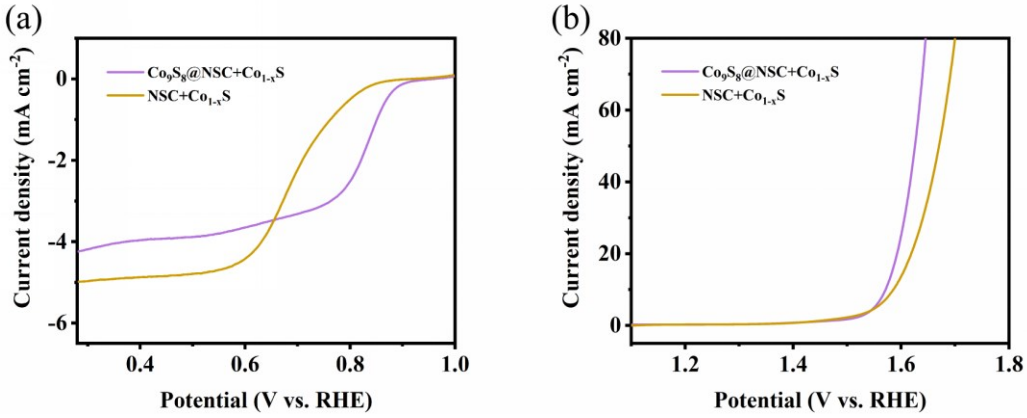

Fig. S10. ORR and OER performance for NSC+$Co_{1-x}S$ and Co_9S_8@NSC+$Co_{1-x}S$ samples.

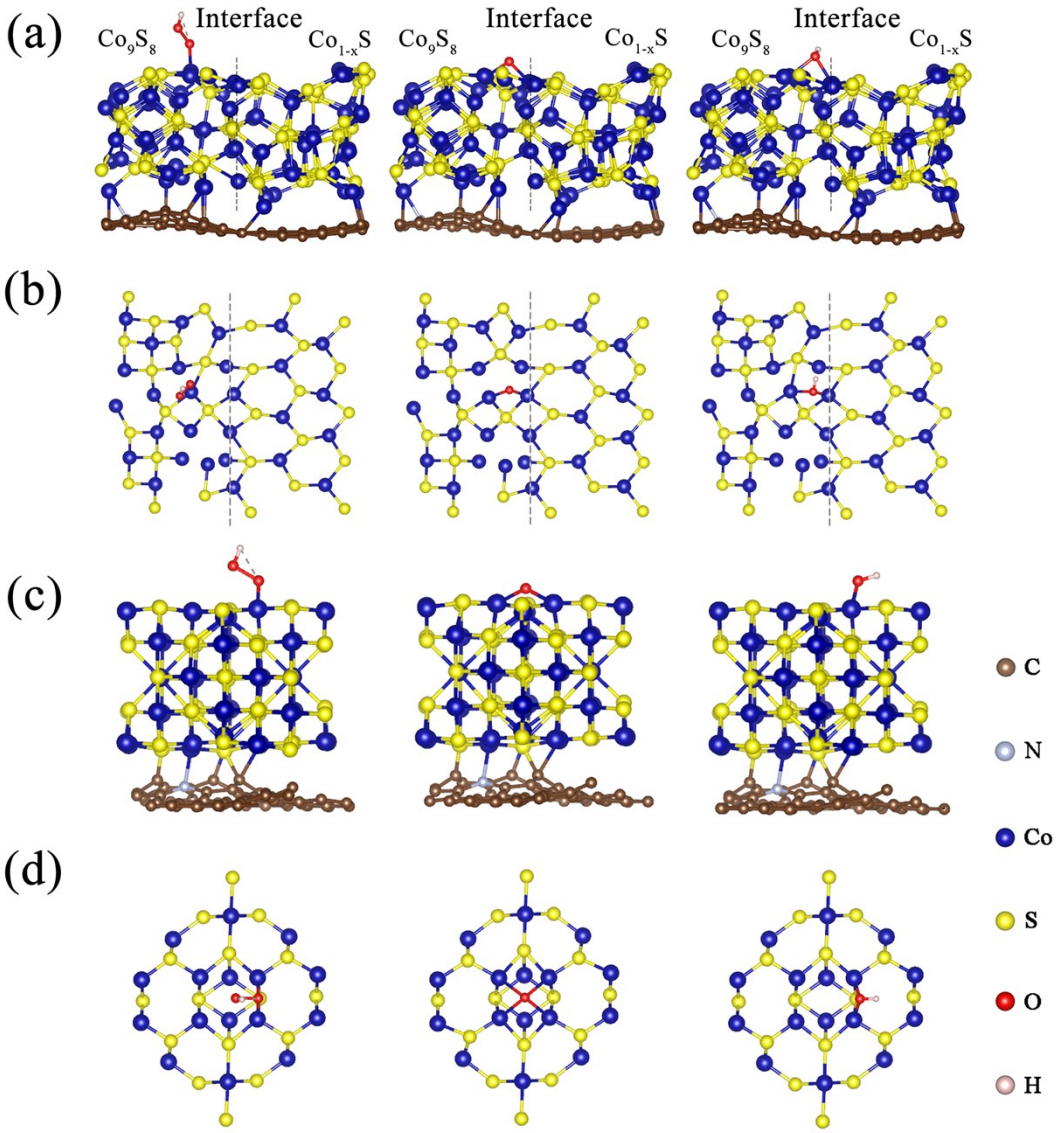

Fig. S11. Optimized atomic configurations of oxygen intermediates (OOH^*, O^* and OH^*) adsorbed on a, b) $Co_9S_8/Co_{1-x}S$@NSC and c, d) Co_9S_8@NSC models from side and top views, respectively.

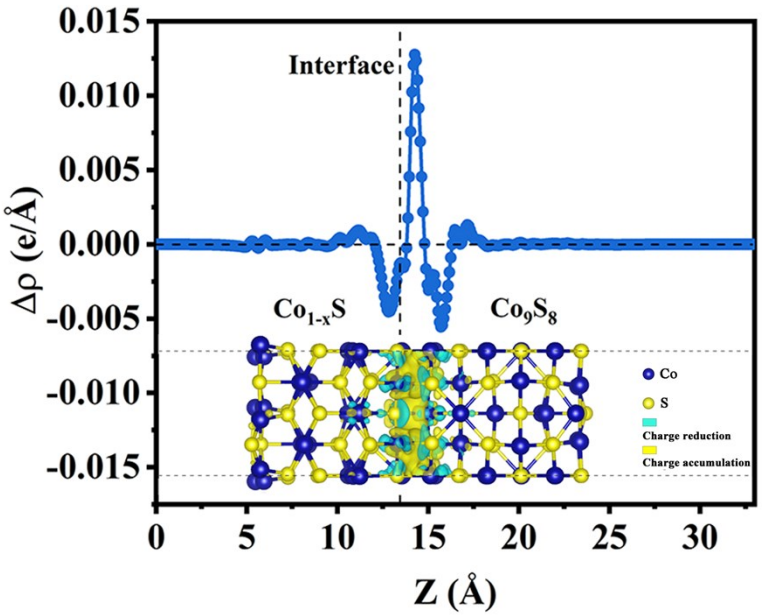

Fig. S12. Charge density difference of $Co_9S_8/Co_{1-x}S$ interface.

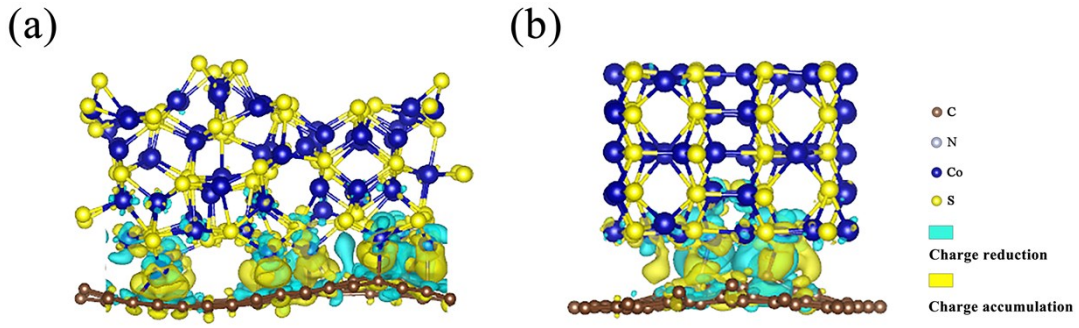

Fig. S13. Charge density difference of a) $Co_9S_8/Co_{1-x}S$ and b) Co_9S_8 bonded with N-containing substrates.

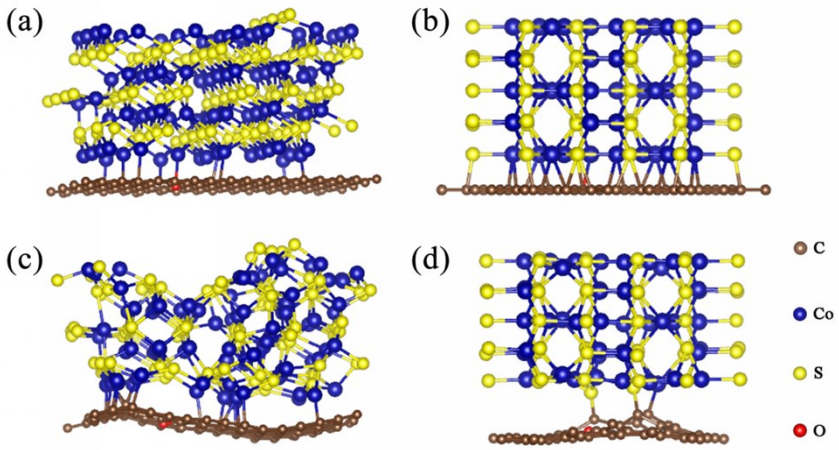

Fig. S14. a) $Co_9S_8/Co_{1-x}S$ and b) Co_9S_8 bonded with O-containing substrates before calculation optimization. c) $Co_9S_8/Co_{1-x}S$ and d) Co_9S_8 bonded with O-containing

substrates after calculation optimization.

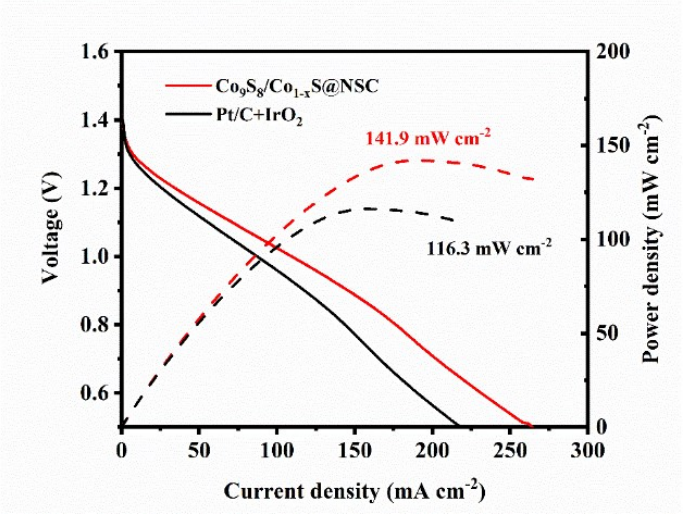

Fig. S15. Polarization curves and corresponding power densities of $Co_9S_8/Co_{1-x}S$@NSC and Pt/C+IrO_2 based zinc–air batteries.

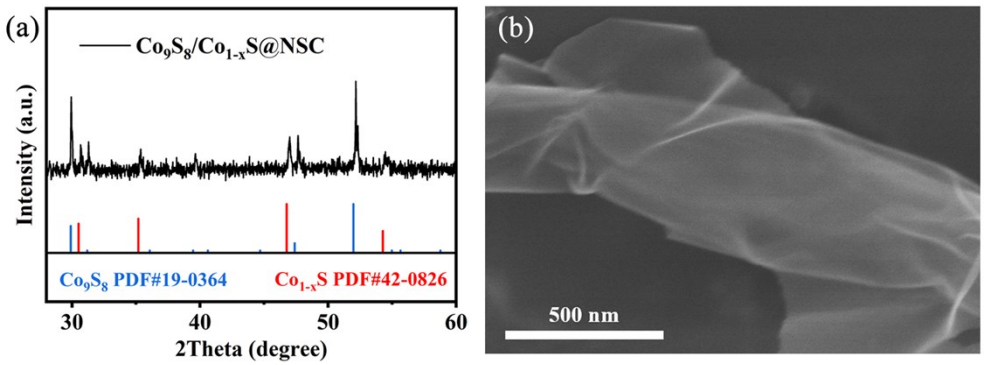

Fig. S16. a) XRD pattern and b) SEM image of $Co_9S_8/Co_{1-x}S$@NSC sample after cycling test in aqueous zinc–air battery.

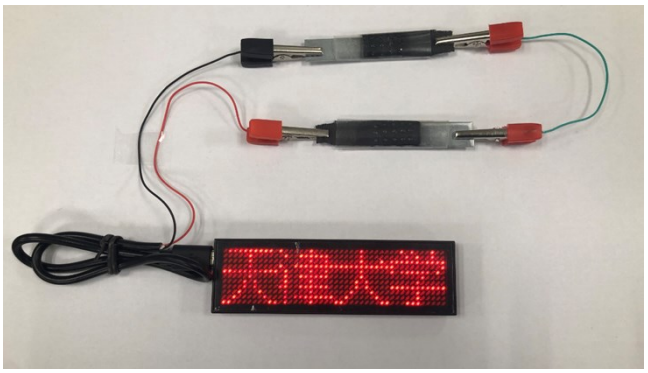

Fig. S17. Two-series connected zinc–air flexible batteries powered LED screen.

Table S1. Summary of ORR and OER results of all electrocatalysts[a]

Catalysts	E_{onset} (V vs. RHE)	$E_{1/2}$ (V vs. RHE)	J_L (mA cm^{-2})	$E_{j=10}$ (V vs. RHE)	ΔE (V vs. RHE)
$Co_9S_8/Co_{1-x}S$@NSC	0.94	0.86	5.50	1.52	0.66
Co_9S_8@NSC	0.90	0.84	4.78	1.57	0.73
NSC	0.89	0.77	4.14	2.01	1.24
Pt/C	0.99	0.86	5.73	–	–
IrO_2	–	–	–	1.62	0.76 (between Pt/C and IrO_2)

[a] E_{onset}, $E_{1/2}$, J_L, $E_{j=10}$ and ΔE denote onset potential, half-wave potential, diffusion-limiting current densities for ORR, potential at current density of 10 mA cm^{-2} for OER and voltage difference between $E_{1/2}$ and $E_{j=10}$, respectively.

Table S2. Comparison of ORR/OER performance for $Co_9S_8/Co_{1-x}S$@NSC with reported cobalt sulfide based bifunctional electrocatalysts.

Catalysts	$E_{1/2}$ (V vs. RHE)	$E_{j=10}$ (V vs. RHE)	ΔE (V vs. RHE)	Ref.
$Co_9S_8/Co_{1-x}S$@NSC	0.86	1.52	0.66	This work
Co_9S_8@NSC	0.865	1.621	0.756	12
Co_9S_8/CS	0.818	1.60	0.782	13
N-Co_9S_8/G	~0.74	1.639	~0.899	14
Co_9S_8/N, S-DLCTs	0.890	1.597	0.707	15
Co_9S_8/N, S-CNTs	0.821	1.609	0.788	16
Co_9S_8/N, P-APC	0.78	1.593	0.813	17
Co_9S_8/CNT	0.82	1.599	0.779	18
Co_9S_8@NS-3DrGO	0.826	1.547	0.721	19

$Co_{1-x}S$/G	0.755	1.579	0.824	20
$Co_{1-x}S$/N–S–G	0.862	1.601	0.739	21
NiS_2/CoS_2–O NWs	0.70	1.465	0.765	22
CoS_2/NSG	0.861	1.623	0.762	23
FeS_2–CoS_2/NCFs	0.81	1.57	0.76	24
CoS_x@NMC	0.79	1.80	1.01	25
CoS_x/Co-NC	0.80	1.54	0.74	26

Abbreviations: CS, carbon spheres; G, graphene; DLCTs, double-layered carbon tubes; CNTs, carbon nanotubes; N, P-APC, alveolate porous N, P-carbon; NS-3DrGO, N-, S-atom-coordinated Co_9S_8 trinary dopants graphene; N–S–G, nitrogen and sulfur co-doped graphene; O NWs, oxygen vacancies dominated nanowires; NCFs, nitrogen-doped carbon nanofiber; NMC, N-doped mesoporous carbon; Co-NC, Co, N-codoped carbon nanotube.

Table S3. Comparison of ORR/OER performance for $Co_9S_8/Co_{1-x}S$@NSC with reported nonprecious metal-based bifunctional electrocatalysts.

Catalysts	$E_{1/2}$ (V vs. RHE)	$E_{j=10}$ (V vs. RHE)	ΔE (V vs. RHE)	Ref.
$Co_9S_8/Co_{1-x}S$@NSC	0.86	1.52	0.66	This work
Co/N-CNTs	0.84	1.62	0.78	27
Fe/C/N	0.83	1.59	0.76	28
CoO	0.85	1.56	0.71	29
Co_3O_4	0.78	1.52	0.74	30
$Co_{0.5}Fe_{0.5}S$@N-MC	~0.81	1.64	~0.83	31
NiFe-LDH/Fe–N–C	0.793	1.539	0.747	32
O-NiFeCo LDH	0.63	1.57	0.94	33

Co_3O_4/Co_2MnO_4	0.68	1.77	1.09	34
Fe@N-C	0.83	1.71	0.88	35

Abbreviations: Co/N-CNTs, Co nanoparticles encapsulated in nitrogen-doped carbon nanotubes; Fe/C/N, Fe doped carbon/nitrogen; N-MC, nitrogen-doped mesoporous graphitic carbon; LDH, layered double hydroxide; O-NiFeCo LDH, trinary LDH containing nickel, cobalt, and iron after preoxidation treatment; Fe@N-C, Fe nanoparticles encapsulated within nitrogen-doped carbon nanoshell.

Table S4. Adsorption free energy of different intermediates adsorbed on Co_9S_8@NSC and $Co_9S_8/Co_{1-x}S$@NSC at 0 V.

G_{ads} (eV)	Co_9S_8@NSC	$Co_9S_8/Co_{1-x}S$@NSC
OOH^*	3.03	3.42
O^*	0.70	1.50
OH^*	−0.35	−0.04

Table S5. The performance of aqueous rechargeable Zn–air batteries with reported cobalt-based electrocatalysts.

Catalysts	OCP (V)	Power density (mW cm^{-2})	Specific capacity (mAh g^{-1})	Cycling stability	Ref.
$Co_9S_8/Co_{1-x}S$@NSC	1.48	141.9	765.4	more than 70 h with stable voltage gap at 5 mA cm^{-2}	This work
NCO	1.45	–	~580	overpotential of ~0.14 V after 50 cycles	36
NiO/CoN PINWs	1.46	79.6	648	negligible voltage fading for 500 min	37
Co_3O_4-doped Co/CoFe	~1.43	~97	727	the voltaic efficiency decreased from initial 64.6% to 46.7% at the 180^{th} cycle	38
$CoIn_2S_4$/S-rGO	1.42	133	745	no obvious voltage variation after 150 cycles	39
Co-Co_3O_4@NAC	1.449	164	721	5.6% increment of voltage gap after cycling for 35 h	40
CE-Co_9S_8@N,S-CM	1.42	14.6	–	the charging and	41

				discharging voltage gap remains stable over 20 h	
Co-Co_9S_8@SN-CNTs	–	93	–	an initial discharge potential of 1.1 V and charge potential of 2.1 V, which remain stable after 90 h	42
Co_9S_8@NSCM	1.45	~179	676	no visible potential decrease after 840 cycles	43
Co_9S_8@TDC	1.50	101.5	–	the discharge voltage enhances slightly (almost negligible) after 20 h cycling	44

Abbreviations: NCO, $NiCo_2O_4$; PINWs, porous interface nanowire arrays; S-rGO, S-doped reduced graphene oxide; NAC, nitrogen-doped active carbon; CE-Co_9S_8@N,S-CM, Co_9S_8-decorated N, S co-doped carbon matrix under confinement effect; Co-Co_9S_8@SN-CNTs, tubular nanostructures composed of Co-Co_9S_8 core and a graphitic carbon shell co-doped with S and N; NSCM, N, S co-implanted carbon matrix; TDC, N, O and S-tridoped carbon.

Supplementary References

1. Y. Tong, P. Chen, T. Zhou, K. Xu, W. Chu, C. Wu and Y. Xie, *Angew. Chem. Int. Edit.* 2017, **56**, 7121–7125.
2. J. Diao, Y. Qiu, S. Liu, W. Wang, K. Chen, H. Li, W. Yuan, Y. Qu and X. Guo, *Adv. Mater.* 2020, **32**, 1905679.
3. X. Yang, K. Li, D. Cheng, W.-L. Pang, J. Lv, X. Chen, H.-Y. Zang, X.-L. Wu, H.-Q. Tan, Y.-H. Wang and Y.-G. Li, *J. Mater. Chem. A* 2018, **6**, 7762–7769.
4. G. Kresse and D. Joubert, *Phys. Rev. B* 1999, **59**, 1758–1775.
5. J. P. Perdew, K. Burke and M. Ernzerhof, *Phys. Rev. Lett.* 1996, **77**, 3865–3868.
6. B. Hammer, L. B. Hansen and J. K. Nørskov, *Phys. Rev. B* 1999, **59**, 7413–7421.
7. P. E. Blöchl, *Phys. Rev. B* 1994, **50**, 17953–17979.
8. H. J. Monkhorst and J. D. Pack, *Phys. Rev. B* 1976, **13**, 5188–5192.
9. H. Huang, J. Zhao and R. Liu, *J. Colloid Interface Sci.* 2021, **582**, 396–404.
10. R. Christensen, H. A. Hansen, C. F. Dickens, J. K. Nørskov and T. Vegge, *J. Phys. Chem. C* 2016, **120**, 24910–24916.
11. X. Han, X. Ling, D. Yu, D. Xie, L. Li, S. Peng, C. Zhong, N. Zhao, Y. Deng and W. Hu, *Adv. Mater.* 2019, **31**, 1905622.
12. S. M. Alshehri, J. Ahmed, A. Khan, M. Naushad and T. Ahamad, *ChemElectroChem* 2018, **5**, 355–361.
13. W. Li, Y. Li, H. Wang, Y. Cao, H. Yu and F. Peng, *Electrochim. Acta* 2018, **265**, 32–40.

14. S. Dou, L. Tao, J. Huo, S. Wang and L. Dai, *Energy Environ. Sci.* 2016, **9**, 1320–1326.
15. C. Hu, J. Liu, J. Wang, W. She, J. Xiao, J. Xi, Z. Bai and S. Wang, *ACS Appl. Mater. Interfaces* 2018, **10**, 33124–33134.
16. L. Chen, W. Yang, X. Liu, L. Long, D. Li and J. Jia, *Nanotechnology* 2018, **30**, 075402.
17. X. Hu, Y. Chen, M. Zhang, G. Fu, D. Sun, J.-M. Lee and Y. Tang, *Carbon* 2019, **144**, 557–566.
18. H. Li, Z. Guo and X. Wang, *J. Mater. Chem. A* 2017, **5**, 21353–21361.
19. Y. Li, Y. Zhou, H. Wen, J. Yang, C. Maouche, Q. Liu, Y. Wu, C. Cheng, J. Zhu and X. Cheng, *Dalton Trans.* 2018, **47**, 14992–15001.
20. Y. Xu, Y. Hao, G. Zhang, X. Jin, L. Wang, Z. Lu and X. Sun, *Part. Part. Syst. Charact.* 2016, **33**, 569–575.
21. X. Qiao, J. Jin, H. Fan, Y. Li and S. Liao, *J. Mater. Chem. A* 2017, **5**, 12354–12360.
22. J. Yin, Y. Li, F. Lv, M. Lu, K. Sun, W. Wang, L. Wang, F. Cheng, Y. Li, P. Xi and S. Guo, *Adv. Mater.* 2017, **29**, 1704681.
23. B. Chen, Z. Jiang, L. Zhou, B. Deng, Z.-J. Jiang, J. Huang and M. Liu, *J. Power Sources* 2018, **389**, 178–187.
24. X. Shi, B. He, L. Zhao, Y. Gong, R. Wang and H. Wang, *J. Power Sources* 2021, **482**, 228955.
25. C. Liu, F. Dong, M. Wu, Y. Wang, N. Xu, X. Wang, J. Qiao, P. Shi and H. Huang, *J. Power Sources* 2019, **438**, 226953.
26. Q. Lu, J. Yu, X. Zou, K. Liao, P. Tan, W. Zhou, M. Ni and Z. Shao, *Adv. Funct. Mater.* 2019, **29**, 1904481.
27. Y. Liu, H. Jiang, Y. Zhu, X. Yang and C. Li, *J. Mater. Chem. A* 2016, **4**, 1694–1701.
28. Y. Zhao, K. Kamiya, K. Hashimoto and S. Nakanishi, *The Journal of Physical Chemistry C* 2015, **119**, 2583–2588.
29. T. Ling, D.-Y. Yan, Y. Jiao, H. Wang, Y. Zheng, X. Zheng, J. Mao, X.-W. Du, Z. Hu, M. Jaroniec and S.-Z. Qiao, *Nat. Commun.* 2016, **7**, 12876.
30. T. Y. Ma, S. Dai, M. Jaroniec and S. Z. Qiao, *J. Am. Chem. Soc.* 2014, **136**, 13925–13931.
31. M. Shen, C. Ruan, Y. Chen, C. Jiang, K. Ai and L. Lu, *ACS Appl. Mater. Interfaces* 2015, **7**, 1207–1218.
32. S. Dresp, F. Luo, R. Schmack, S. Kühl, M. Gliech and P. Strasser, *Energy Environ. Sci.* 2016, **9**, 2020–2024.
33. L. Qian, Z. Lu, T. Xu, X. Wu, Y. Tian, Y. Li, Z. Huo, X. Sun and X. Duan, *Adv. Energy Mater.* 2015, **5**, 1500245.
34. D. Wang, X. Chen, D. G. Evans and W. Yang, *Nanoscale* 2013, **5**, 5312–5315.
35. J. Wang, H. Wu, D. Gao, S. Miao, G. Wang and X. Bao, *Nano Energy* 2015, **13**, 387–396.
36. M. Prabu, K. Ketpang and S. Shanmugam, *Nanoscale* 2014, **6**, 3173–3181.
37. J. Yin, Y. Li, F. Lv, Q. Fan, Y.-Q. Zhao, Q. Zhang, W. Wang, F. Cheng, P. Xi and S. Guo, *ACS Nano* 2017, **11**, 2275–2283.
38. T. Li, Y. Lu, S. Zhao, Z.-D. Gao and Y.-Y. Song, *J. Mater. Chem. A* 2018, **6**, 3730–3737.
39. G. Fu, J. Wang, Y. Chen, Y. Liu, Y. Tang, J. B. Goodenough and J.-M. Lee, *Adv. Energy Mater.* 2018, **8**, 1802263.

40. X. Zhong, W. Yi, Y. Qu, L. Zhang, H. Bai, Y. Zhu, J. Wan, S. Chen, M. Yang, L. Huang, M. Gu, H. Pan and B. Xu, *Appl. Catal. B-Environ.* 2020, **260**, 118188.
41. L. Meng, L. Zhan, H. Jiang, Y. Zhu and C. Li, *Catal. Sci. Technol.* 2019, **9**, 5757–5762.
42. H. Han, Z. Bai, T. Zhang, X. Wang, X. Yang, X. Ma, Y. Zhang, L. Yang and J. Lu, *Nano Energy* 2019, **56**, 724–732.
43. Y. Li, W. Zhou, J. Dong, Y. Luo, P. An, J. Liu, X. Wu, G. Xu, H. Zhang and J. Zhang, *Nanoscale* 2018, **10**, 2649–2657.
44. J.-Y. Zhao, R. Wang, S. Wang, Y.-R. Lv, H. Xu and S.-Q. Zang, *J. Mater. Chem. A* 2019, **7**, 7389–7395.